Remote Sensing Applications: Society and Environment 42 (2026) 101963

Contents lists available at ScienceDirect

Remote Sensing Applications: Society and Environment

journal homepage: www.elsevier.com/locate/rsase

Forecasting the time of failure of tailings dams and Heap Leach Facilities through satellite InSAR data: myth or reality?

Stefano Szakolczai [a,*], Luca Piciullo [b], Regula Frauenfelder [b], Malte Vöge [b], Tommaso Carlà [a], Emanuele Intrieri [a]

[a] Department of Earth Sciences, Università degli Studi di Firenze, Via Giorgio La Pira 4, 50121, Florence, Italy
[b] Norwegian Geotechnical Institute (NGI), Sognsveien 72, 0855, Oslo, Norway

ARTICLE INFO

Keywords:
Tertiary creep methods
TSF
Early warning systems
Reiterative algorithm
Prospective monitoring

ABSTRACT

This paper addresses the complex challenge of forecasting the Time of Failure (ToF) for Tailings Storage Facilities (TSFs) and Heap Leach Facilities (HLFs) using satellite-based Interferometric Synthetic Aperture Radar (InSAR) data. TSF and HLF structures can be susceptible to different failure modes, some of which can result in sudden instability due to the tailings' contractive and brittle behaviour. Moreover, the infrequent satellite passes can limit the ability to detect rapid changes or deformations in these structures, potentially reducing the effectiveness of monitoring efforts. Some recent papers propose predicting brittle failures in such structures using tertiary creep-based forecasting methods. However, this often requires a subjective procedure, and the results yielded are sometimes different and sometimes contradictory. To fully exploit the predictive potential of satellite InSAR data, a statistical multi-model methodology is introduced, with a primary focus on providing both quantitative estimates of the predictions and forecasting reliability. Through this methodology, different levels of warnings are issued. Low confidence alert would have been reached for Cadia up to 2 months in advance, whereas the highly confident one 12 days prior to the collapse. For Feijão moderate confidence alert would have been reached 39 days before failure. Special emphasis is placed on the evolution of failure risk in a simulated prospective manner, reproducing operational monitoring conditions. Our findings highlight the need for multiple technologies to accurately monitor such structures and justify the use of satellite InSAR for hazard screening.

1. Introduction

Tailings are by-products of the mining industry, consisting of a mixture of crushed rock and processing fluids that remain after the economic extraction of metals, ores, mineral fuels, or coal from a mineral resource (Kossoff et al., 2014). Tailings dams, referred to here as Tailings Storage Facilities (TSFs), are structures designed to retain these materials and are typically constructed using the coarser fraction of the tailings themselves. Historical data indicate that TSFs are highly vulnerable to collapse, with an estimated 10 per cent experiencing stability problems (Franks et al., 2021). A dam breach can release large amounts of tailings into streams, posing a significant environmental threat (Kossoff et al., 2014; Motsau and van Wyk, 2022). Over the last century, more than 250 collapses have occurred, releasing up to 250 million cubic meters of tailings and resulting in approximately 2650 human casualties (Piciullo et al.,

* Corresponding author. Via Giorgio La Pira 4, 50121, Florence, Italy.
E-mail address: istvan.szakolczai@unifi.it (S. Szakolczai).

https://doi.org/10.1016/j.rsase.2026.101963
Received 13 October 2025; Received in revised form 9 February 2026; Accepted 7 March 2026
Available online 9 March 2026

2022; Hudson-Edwards et al., 2024). Although the scale of these disasters is enormous, many of them were avoidable (Davies, 2002; Clarkson et al., 2021), and TSFs are among the largest and least stable anthropogenic structures (Bowker and Chambers, 2015). Notable recent events include the Fundão TSF failure (Brazil) in 2015, which led to 19 fatalities (Carmo et al., 2017), the Feijão 'Dam I' failure (Brazil) in 2019, which resulted in at least 260 fatalities (Cambridge and Shaw, 2019; Rotta et al., 2020), and the Jagersfontein TSF failure (South Africa) in 2022, which resulted in two fatalities (Marais et al., 2024).

Enormous structures that share the same failure hazard are Heap Leach Facilities (HLFs), as evidenced by two recent major failures in Turkey and Canada (BBC, 2024; Yukon, 2024). TSF and HLF failures highlight significant challenges for mining practices. Often located near fragile communities and ecosystems, these facilities require continuous, real-time monitoring (Clarkson et al., 2021).

To analyze TSF and HLF failures, we focus on Multi-temporal satellite Interferometric Synthetic Aperture Radar (Mt-InSAR) data, as its usefulness has been widely recognized in both natural hazards and infrastructure instability (Sousa and Bastos, 2013; Ishwar and Kumar, 2017; Solari et al., 2020; Dai et al., 2021; Raspini et al., 2022; Casagli et al., 2023). The technique enables ground deformations detection with millimetric accuracy (Ferretti et al., 2011), offering extensive spatial coverage, even over remote locations (Dai et al., 2020). Moreover, continuous temporal information enables the development of systematic failure forecasting models (Raspini et al., 2018). However, it must be reported that the critical limitations inherent in satellite InSAR for natural slope monitoring (Lacroix et al., 2022) are furthermore exacerbated in a mining environment, primarily due to the continuous remodeling of the land. Indeed, the main critical issues, such as the loss of coherence due to phase unwrapping problematic of phase aliasing (Manconi, 2021), the non-linear behaviors in time of the displacement rate (alternance of stable/unstable phases), and the poor reliability of the signal due to sensor/structure geometry, need to be addressed in considering satellite InSAR to monitor TSFs (Rana et al., 2024) and HLFs. This is particularly important given that InSAR-derived analysis can produce false alerts, as reported in previous studies (Milillo et al., 2019; Lanari et al., 2020).

Nevertheless, recent studies have demonstrated the potential of using Mt-InSAR in analyzing TSF failures, reaching similar conclusions: although the revisit time of satellite InSAR poses a challenge for monitoring brittle failures, it can be an effective tool for hazard screening as it can capture the entire target area, whereas point-based monitoring systems are limited to less densely distributed Measurement Points (MPs) (Bayaraa et al., 2022; Mirmazloumi et al., 2023; Rana et al., 2024). Particular attention has been devoted to the concept of estimating the Time of Failure (ToF) and assessing how far in advance failure might be foreseeable from satellite (Intrieri et al., 2018). In particular, studies have investigated ToF predictions for TSFs in Australia (Carlà et al., 2019a; Thomas et al., 2019), Brazil (F. Gama et al., 2020; Grebby et al., 2021), and China (Duan et al., 2023; Su et al., 2024), with particularly promising results reported in the Australian example.

The underlying premise of forecasting methods is rooted in the concept that a slope may undergo deformation before rupture, a phenomenon described by the classic creep theory (Saito and Uezawa, 1961; Tavenas and Leroueil, 1981).

These methods were originally developed for natural slopes and assume constant loading conditions. Such assumptions may limit their applicability to brittle or structural failures, which may not follow classical creep behavior (Rose and Hungr, 2007; Mufundirwa et al., 2010). Nevertheless, tertiary creep methods have been successfully applied to predict the failure of TSFs (Carlà et al., 2019a), medieval walls (Carlà et al., 2017), and even to predict volcanic eruptions (Voight, 1988). These examples support extending slope stability forecasting methods to structures such as TSFs and HLFs.

Thus, in this contribution, the main approximation lies in assuming that accelerating deformation trends, regardless of the specific physical mechanism or loading conditions, can be analyzed with creep forecasting analysis, provided that a measurable acceleration trend is present in the monitoring data (Intrieri and Gigli, 2016). In addition, absence of constant external loading does not necessarily preclude successful forecasting, further supporting the applicability of such approaches to complex and evolving systems (Intrieri and Gigli, 2016).

Although predicting retrospectively the ToF yields good alignment with the actual failure time, this may require knowledge of when the failure has effectively occurred. In many cases, this attitude necessitates a post-tuning phase (Leinauer et al., 2023), which is not suitable in emergency situations. In recent years, therefore, attention has been devoted to the real-time applications of ToF forecasting in order to utilize it practically (Leinauer et al., 2023; Sharifi et al., 2024; Tordesillas et al., 2024; Zhang et al., 2025).

When precise ToF estimation is not feasible, threshold-based Early Warning Systems (EWSs) can provide valuable support for risk mitigation (Intrieri et al., 2012). In particular, satellite InSAR-based EWSs have gained increasing attention due to their cost-effectiveness, systematic acquisition, and wide spatial coverage (Raspini et al., 2018; Navarro et al., 2020; Festa et al., 2022; Calò et al., 2024).

In this context, the present study applies a reiterative forecasting framework to satellite InSAR time series. Building on the methodology proposed by Intrieri & Gigli (2016), we introduce a multi-step forecasting and alerting strategy designed to evaluate both prediction reliability and warning lead time under realistic monitoring conditions. The main improvement over previous applications of the methodology, which tested predictability of diverse failures using different forecasting methods, lie in the explicit quantification of failure risk evolution and the definition of multiple warning levels, providing timely information to support decision-making.

The methodology, combined with InSAR satellite data, is being applied for the first time to TSFs and an HLF, which are characterized by a pre-failure window that can be hidden by noise, and if present, can be very short. Our iterative approach could address such concerns by prospectively analyzing the predictive scenario and boosting the subtle pre-failure information. Moreover, different warning levels can provide timely information to decision-makers. For early warning purposes, we focus on kinematics data only, as this may be the most readily accessible information (Zhang et al., 2025). This is further justified by the fact that particular geomechanical behavior may be hinted by kinematics (Intrieri and Gigli, 2016). Thus, the methodology proposed here can be a valuable tool for detecting pre-failure windows in real time, aligning with disaster risk reduction plans to save lives and mitigate economic damage (Intrieri et al., 2021).

Finally, a further objective of this research is to clarify whether ToF forecasting using satellite InSAR data can be effectively applied. Indeed, scholars reached some disagreements about the possibility of predicting Feijão 'Dam I' failure through tertiary-creep methods. In fact, it was reported that a warning of failure could have been issued as early as 40 days before failure (Grebby et al., 2021), while others claimed that the confidence in such forecast was low (Gama et al., 2020), and that the signals obtained are not statistically significant compared to the InSAR noise, revealing no precursor deformation in the two months preceding the collapse (Holden et al., 2020). By applying a comprehensive and objective statistical methodology, we aim to resolve these differing results, which are most likely due to subjective approaches.

In summary, this study introduces a satellite-based Mt-InSAR forecasting framework that integrates tertiary creep methods into a simulated prospective early-warning strategy. The methodology is calibrated and validated using multiple historical failure and non-failure cases to assess its practical feasibility. The approach is then applied to five large mining structures distributed across different continents: Cadia NTSF (Australia), Çöpler HLF (Turkey, Asia), Feijão 'Dam B1' TSF (Brazil, South America), Jagersfontein TSF (South Africa), Żelazny Most TSF (Poland, Europe).

2. Methodology

Following the framework presented in Intrieri & Gigli (2016), the basic concept behind the methodology adopted here is the iterative calculation of the Time of Failure, ToF, through various forecasting methods at each timestamp. Henceforth, we define this methodology as the Reiterative Algorithm, RA. With timestamp, we refer to the time value at which a measurement was registered. With satellite InSAR data, this corresponds to the time when the satellite acquires a new image, which in the case of Sentinel-1 constellation is 6 to 12 days.

At each timestamp and for each new displacement data acquired by the sensor, the RA workflow performs the following steps: (a) iterative computation of the ToF predictions through multiple forecasting methods using all available data up-to-date; (b) filtering of predictions and statistical evaluation of their variability; (c) computation of the Failure Score (FS); (d) estimation of forecasting uncertainty using the Standard Error of the Mean (SEM); (e) evaluation of the FS and/or FS-to-noise ratio and issuance of warning levels based on persistent trends; (f) identification of Failure Trend conditions when different forecasting methods provide corroborating evidence of prediction convergence.

In this work, forecasting confidence is evaluated by the variability of ToF predictions: a reduction in prediction variability and convergence toward a specific failure time are interpreted as indicators of an increasing likelihood of collapse.

2.1. Forecasting methods

Based on the relationship between deformation and time before failure, various empirical methods have been developed to predict the instant at which collapse may occur (Saito, 1969; Fukuzono, 1985; Voight, 1988; Mufundirwa et al., 2010). In this article, we focus on Saito (1969) and Fukuzono (1985) forecasting methods, which have shown promising results (Intrieri and Gigli, 2016). From now on, the application of the abovementioned methods in RA algorithm will be defined as RAS and RAF, respectively.

2.1.1. RAS ToF equation

Saito's empirical graphical approach based on the tertiary creep theory (Saito, 1969) can also be expressed in a numerical format (Intrieri et al., 2019). From a cumulative displacement time series with N observations, $A_{n+1} = (t_{n+1}, D_{n+1})$ with $n = \{0, 1, 2, \ldots, N\text{-}1\}$, the ToF of the slope can be obtained using (Eq. 1):

$$ToF = \frac{\tau^2 - \mathrm{T}t_{n+1}}{2\tau - (\mathrm{T} + t_{n+1})}, \tag{1}$$

where ToF represents the predicted ToF, T is the time corresponding to the cumulative displacement D, t_{n+1} is the time corresponding to the cumulative displacement D_{n+1}, and τ is the time corresponding to half the displacement between D and D_{n+1}.

2.1.2. RAF ToF equation

The graphical approach for Fukuzono's inverse velocity method (INV), which is widely used in scientific literature for its simplicity, has also a numerical format (Fukuzono, 1985), that can be summarized in (Eq. 2):

$$ToF = \frac{t_{n+1}(\Lambda_T) - \mathrm{T}(\Lambda_{n+1})}{\Lambda_T - \Lambda_{n+1}}, \tag{2}$$

where ToF is the predicted ToF, T and t_{n+1} are data acquisition time values selected from the cumulative displacement time series and Λ_T and Λ_{n+1} represent the reciprocal of velocities (1/v) at timestamps T and t_{n+1}, respectively.

2.2. Reiterative Algorithm, RA

Let a cumulative displacement time series have N observations. The data observation gathered are defined as A_{n+1} (t_{n+1}, d_{n+1}), with $n = \{0,1, 2, \ldots, N\text{-}1\}$ (Fig. 1, step 1). The first observation (n = 0) is defined as $A_1(t_1, d_1)$, where t_1 denotes the time when data collection begins and d_1 the displacement measured.

From this time series, let T and t be two timestamps such that $T < t$. Predictions are computed using RAS (Eq. 1) and RAF (Eq. 2) (step 2). Keeping T fixed, successive timestamps and displacement values are used to compute additional predictions (step 3, T is set as t_1). Once all forecasts associated with T are generated, the next timestamp is selected as the new T, and the procedure is repeated (*re-iterated*) (step 4). This sequential procedure continues until all timestamps, except the last, have been used as T to generate N-1 prediction series (step 5).

Each prediction is denoted $ToF_{m,T,n}$, where m identifies the forecasting method used (s for Saito and f for Fukuzono), T is the starting timestamp, and n is the n-value of the timestamp (t_{n+1}) used to compute the ToF, hereinafter referred to as the *time of prediction*.

At each timestamp, the totality of forecasted ToF computed using the available displacement data are considered together to evaluate prediction convergence and therefore forecasting confidence.

2.2.1. RA example

Consider a cumulative displacement time series containing four observations $(N=4)$:, $A_1(d_1, t_1)$, $A_2(d_2, t_2)$, $A_3(d_3, t_3)$, $A_4(d_4, t_4)$ (Fig. 2). First, t_1 is fixed as the starting timestamp T, and t_2, t_3, and t_4 are used to generate three ToF predictions with the RAS (Eq. 1), $ToF_{s,\ t1,\ (1,2,3)}$, and three with RAF (Eq. 2), $ToF_{f,\ t1,\ (1,2,3)}$. Next, t_2 is fixed as the new T, and timestamps t_3 and t_4 are used to compute two predictions per methods, namely $ToF_{s,\ t2,\ (2,3)}$ and $ToF_{f,\ t2,\ (2,3)}$. Finally, t_3 is fixed as T, and only t_4 is used to compute a single ToF prediction per method: $ToF_{s,\ t3,\ 3,}$ and $ToF_{f,\ t3,\ 3}$.

Fig. 2 illustrates the cumulative displacement time series and point $B\ (\delta,\ \tau)$, which is used to extrapolate τ. This parameter, along with t_1 and t_4, is required to compute the $ToF_{s,\ t1,\ 3}$ through RAS. For the corresponding RAF prediction, $ToF_{f,\ t1,\ 3}$, only the reciprocal velocities at timestamp t_1 and t_4 and their corresponding time values are required.

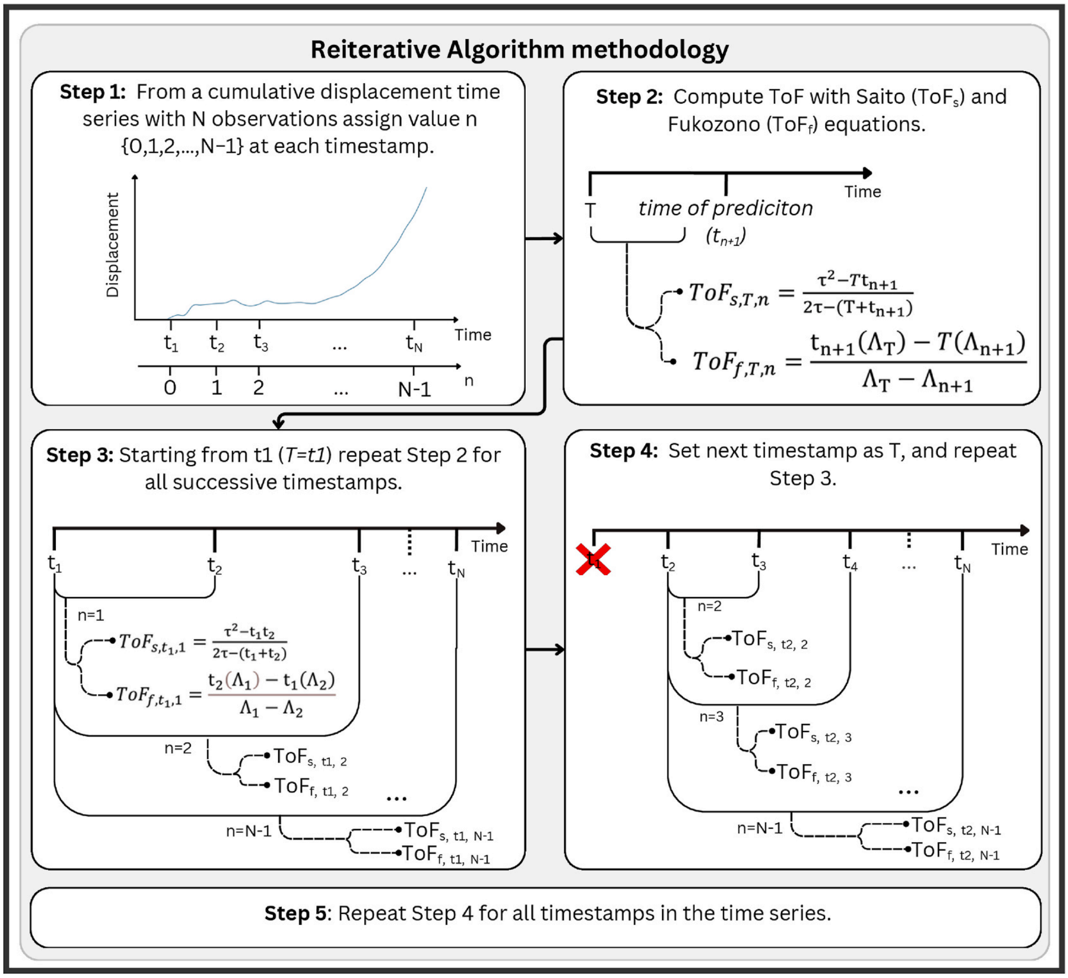

Fig. 1. Scheme of the RA methodology.

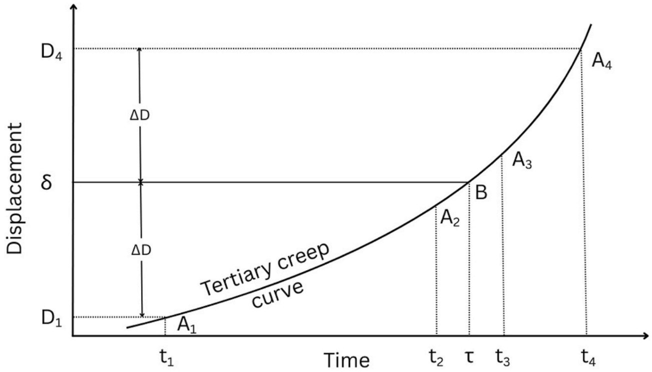

Fig. 2. Cumulative displacement time series showing a tertiary creep trend. Four observations are selected: A_1 (d_1, t_1), A_2 (d_2, t_2), A_3 (d_3, t_3), A_4 (d_4, t_4). In particular, the methodology used to compute ToF $_{s,\ t1,\ 3}$ through Eq. (1) is illustrated.

2.2.2. Predictions filtering

The *re*-iterative procedure may generate numerous ToF predictions. To retain only forecasts that are meaningful in terms of ToF forecasting, the results are subsequently filtered with two criteria: the first eliminates predictions that anticipate the prediction time (which does not make sense for ToF forecasting), and the second removes predictions that deviate by one standard deviation from the mean (defined as outliers).

2.3. Prediction plot

The predictions are displayed in prediction plots, with the forecasted ToF on the y-axis and the time of prediction on the x-axis. At each timestamp, only displacement data acquired at that time, along with all previous data, are used to simulate a real-case scenario.

The variability of the predictions is considered a proxy for the forecast's confidence. If the SD is decreasing and the forecasts approach the average, the likelihood of failure increases. This is quantified using the Failure Score, introduced below.

2.4. Failure score, FS

The FS is a dimensionless parameter introduced to quantify the convergence of predictions and thus the relative likelihood of failure. At each timestamp *t*, the standard deviation (SD) of the forecasts (SD_t) is compared with the distribution of the SD of all previous forecasted values (SD_{tot}). Percentile-based thresholds are used to classify risk levels and assign FS values.

Thresholds were calibrated using ten failure case studies and four non-failure case studies representing characteristic deformation behaviors (step-like, seasonal, steady creep, and stable conditions). Details of the datasets are provided in Tables 1 and 2.

The value of FS depends on how much the SD_t variability decreases or increases relative to SD_{tot}. To quantify such variability, we

Table 1
Failure case studies used for RA validation and FS threshold calibration.

Name	Monitoring technique	# of data acquisition	# of alerts	Failure trend detected (from–to)	Actual ToF	Lead time before failure (days)	Alert [a]	Ref [b]
Agoyama	Unknown	49	1	Nov 20, 1972 → failure	Dec 12, 1972	13	TP	1
Arvigo ['POT5_3']	Telejointmeter	76	1	May 15, 2007 08:30 → failure	May 28, 2007 20:00	14	TP	2
Gallivaggio	GB-InSAR	208	8 (7FP)	May 15, 2018 06:33 → failure	May 29, 2018 16:05	15.4	TP	3
Hogart [J2]	Extensometer	285	11 (10FP)	Jun 10, 1975 → failure	Jun 26, 1975	17	TP	4
Kagemori [1_mm]	Measuring tape	443	15 (14FP)	Sep 12, 1973 → failure	Sep 20, 1973	9	TP	5
Mt. Beni [15-13]	Extensometer	39	1	Nov 07, 2002 11:30 → failure	Dec 28, 2002	44	TP	6
Nevis bluff	Survey markers	266	2 (1FP)	Jan 29, 1975 → failure	Jun 14, 1975	137	TP	7
Ohto	Extensometer	90	1	Aug 01, 2004 → failure	Aug 10, 2004	10	TP	8
Open Pit Slope	EDM prisms	70	4 (3FP)	Jul 19, 1990 → failure	Jul 26, 1990	8	TP	9
Xinmo	Sat-InSAR	45	2 (1FP)	May 26, 2017 → failure	Jun 24, 2017	30	TP	10

[a] TP: failure detected; FP: false alarm; TN: correct rejection; FN: missed failure.
[b] 1: Hayashi and Yamamori (1991); 2: Leinauer et al. (2023); 3: Carlà et al. (2019b); 4: Brawner and Stacey (1979); 5: Yamaguchi and Shimotani (1986); 6: Gigli et al. (2011); 7: Brown et al. (1980); 8: Suwa et al. (2010); 9: Ryan and Call (1992); 10: Intrieri et al. (2018).

define four thresholds that are updated at each timestamp. The value of SD_t within the thresholds establishes the risk of failure.

In particular, for:

- $SD_t > SD_{tot,q95}$: the risk of failure is 'Very Low' and a value of '-2' is attributed to FS;
- $SD_{tot,q50} < SD_t \leq SD_{tot,q95}$: the risk of failure is considered 'Low', and FS = '-1';
- $SD_{tot,q30} < SD_t \leq SD_{tot,q50}$: the risk of failure is considered 'Moderate', and FS = '+3';
- $SD_{tot,q15} < SD_t \leq SD_{tot,q30}$: the risk of failure is considered 'High', and FS = '+6';
- $SD_t \leq SD_{tot,q15}$: the risk of failure is considered 'Very High', and FS = '+9'.

In this way, the FS is structured to decrease constantly if no convergence of the forecast is observed, and similarly, increases as soon as convergence is shown. The value of FS increases weightedly as the variability of SD decreases.

2.5. Standard error of the mean, SEM

To evaluate the confidence in the predictions, the Standard Error of the Mean, SEM, is used. The SEM quantifies uncertainty in estimate of the mean (Barde and Barde, 2012) and is used here to quantify the prediction confidence. At each timestamp the SEM is computed through:

$$SEM_t = \frac{SD_t}{\sqrt{N_t}} \tag{3}$$

where SD_t is the standard deviation of the predictions made at timestamp t, and N_t is the number of predictions made at the same timestamp. Lower SEM value indicate that the forecasted values converge to their mean, corresponding to low dispersion and enhanced confidence, whereas higher SEM values indicate greater dispersion and reduced confidence.

2.6. Signal-to-noise ratio, SNR

To further assess reliability, a Signal-to-Noise (SNR) is defined as the ratio between the cumulative FS and SEM:

$$SNR_t = \frac{\sum_{i=0}^{t} FS_i}{SEM_t} \tag{4}$$

where FS_i is the instantaneous failure score at time i, and SEM_t is the standard error of the ensemble predictions at time t.

Positive SNR values indicates that the warning signal is predominant over the predictions uncertainty, whereas low or negative values indicate weak or unreliable warning signals.

2.7. Early warning

2.7.1. Low to moderate confidence alerts

Based solely on one forecasting algorithm, two scenarios of early warning are identified:

- A first level of warning (yellow alert – low confidence) is issued when the FS increases persistently over two consecutive timestamps.
- A second level of warning (red alert – moderate confidence) when, alongside an increase in the FS, an increase of the SNR is also observed.

Alerts are activated only when conditions persist for two consecutive timestamps and remain active until conditions are not met for two consecutive timestamps, ensuring temporal robustness.

By applying the Early Alert framework to RA predictions, first-level warnings may be issued even when the SEM is not decreasing. A scattered or highly variable SEM reduces the confidence associated with the alert; however, to minimize the probability of false negatives and maintain sensitivity to acceleration in early stages, also low confident alerts are retained. False alerts will be further

Table 2
Non-failure case studies used for RA training and FS threshold calibration.

Name [a]	Monitoring Technique	# of data acq.	Failure Trend detected (From–To)	Alert[b]
Test 1 (step-like deformation)	Sat-InSAR	45	None	TN
Test 2 (seasonal motion)	Sat-InSAR	45	None	TN
Test 3 (constant creep)	Sat-InSAR	45	None	TN
Test 4 (seasonal stable)	Sat-InSAR	45	None	TN

[a] Non-failure cases have been extracted from a satellite InSAR dataset.
[b] TP: failure detected; FP: false alarm; TN: correct rejection; FN: missed failure.

discussed in discussion section.

In order to achieve an even higher level of confidence, an additional alert is defined: the Failure Trend.

2.7.2. *High confidence alert – failure trend*

A Failure Trend is identified when one forecasting method reaches a red alert, and the other reaches at least a yellow alert. This condition indicates that both forecasting approaches are detecting an acceleration and represents the highest alert confidence level.

2.8. *'Simulated' prospective analysis*

All alerts and predictions are evaluated prospectively in a simulated setting. At each timestamp, only displacement data acquired at that timestamp (*time of prediction*), along with all previous data, are used to simulate a real-case scenario. A prediction plot that changes continuously at each timestamp, can thus be used to evaluate the evolution of failure risk alongside the forecasting confidence. Indeed, a decrease in variability and convergence of predictions toward a common ToF are interpreted, within this framework, as evidence of increasing failure likelihood.

2.9. *Site-specific calibration phase*

To reduce false positives (FPs), an initial pre-training phase is defined during which the FS is not computed. A minimum of ten predictions is required before FS starts to be computed. This is followed by a site-specific training phase lasting five consecutive timestamps after the start of FS computation. After this period, the alerts are considered reliable.

This procedure reduces FPs and improves lead time for true positives (TPs) detections.

3. Materials

In this contribution, we analyzed the pre-failure deformations of three TSFs, Cadia NTSF – Northern Tailings Storage Facility (Australia), Feijão 'Dam B1', hereinafter Feijão (Brazil), and Jagersfontein (South Africa), and one HLF at Çöpler gold mine (Turkey), all of which catastrophically failed. In addition, Zelazny Most was also analyzed as a non-failure case in order to evaluate the model performance under conditions of intense deformation without collapse. Comprehensive case study descriptions are reported in the Supplementary Materials.

3.1. *Mt-InSAR*

Decorrelation in SAR imaging refers to the physical phenomenon in which radar echoes do not interact with scattered targets in the same manner (Zebker and Villasenor, 1992). When comparing SAR images phases using Differential InSAR (D-InSAR), decorrelation effect may arise, from atmospheric disturbance (Massonnet and Rabaute, 1993), topography, or temporal changes, potentially altering and compromising the quality of the final results.

To mitigate these effects, Multi-temporal InSAR (Mt-InSAR) techniques were developed, exploiting stacks of SAR images to improve signal coherence and displacement accuracy (Raspini et al., 2022). These approaches include: (i) Persistent Scatter Interferometry (PSI) (Ferretti et al., 2011); (ii) Small Baseline Subset technique (SBAS) (Berardino et al., 2002) which leverages Distributed Scatterers using small spatial and temporal baselines to reduce spatial decorrelation; and (iii) hybrid approaches combining both strategies, such as SqueeSAR (Ferretti et al., 2011), StaMPS (Hooper, 2008), and E-SBAS (Famiglietti et al., 2024).

Such MT-InSAR approaches can exploit long sequences of SAR image sequences to mitigate phase-correlation issues, including decorrelation, noise, and orbital errors.

Table 3
Analyzed Sentinel-1 datasets.

Case study	No. of images	Pass	Incidence Angle of LOS (°)	Time span	ToF	Temporal resolution (days)
Cadia NTSF (Australia)	80	Descending	33	Jan 01, 2015 – Feb 25, 2018	Mar 09, 2018	12,7
Çöpler (Turkey)	87	Ascending	32.2	Aug 02, 2021 – Feb 06, 2024	Feb 13, 2024	10,6
Feijão (Brazil)	108	Descending	32	May 01, 2015 – Jan 22, 2019	Jan 25, 2019	12,6
Jagersfontein (South Africa)	112	Ascending	43,54	Jan 06, 2019 – Aug 30, 2022	Sep 11, 2022	11,9
Zelazny Most (Poland)	141	Descending	38	Jan 04, 2018 – May 05, 2020	No failure	6,04

3.2. Data processing

Sentinel-1 Single Look Complex (SLC) images acquired in Interferometric Wide (IW) swath mode were used to retrieve displacement time series. Acquisition geometries were chosen to provide sufficiently coherent, spatially and temporally continuous interferograms and an LOS suitable for observing the expected direction of motion. SAR data were downloaded from the Alaska Satellite Facility (ASF) https://search.asf.alaska.edu/or the Copernicus hub https://browser.dataspace.copernicus.eu/.

As summarized in Table 3, the time coverage of the images was selected to be at least three years before failure, while in Zelazny Most case, two years covering the monitored deformation.

Mt-InSAR processing was performed using the SARscape® v5.7.0 software. Atmospheric phase delays were corrected using the Generic Atmospheric Correction Online Service for InSAR (GACOS) (http://www.gacos.net/index.html), and residual topographic phase component was removed using the ALOS World 3D digital elevation model (JAXA).

SBAS processing chain (Berardino et al., 2002) was applied to all case studies except for Cadia, in which Enhanced SBAS (E-SBAS) (Famiglietti et al., 2024) was used. Indeed, in this case, E-SBAS improved the stability of the time series.

Multilooking was applied primarily to obtain approximately square pixels of about 15 m, without further spatial downsampling. Under the challenging coherence conditions typical of mining environments, low coherence thresholds were adopted: 0.1 for all cases except Zelazny Most (0.2). For Cadia, a PSI coherence threshold of 0.75 was also applied.

3.3. Post-processing data interpretation

MPs were imported into a GIS environment and overlaid with pre- and post-failure satellite imagery to delineate the source area of failure. Displacement time series corresponding to MPs located within these areas and exhibiting significant ($|V_{LOS}| > 10$ mm/year) were extracted.

To reduce noise, the mean displacement time series was smoothed with 3-point moving average before being used as input in the RAF and RAS algorithms. As shown in Carlà et al. (2017), this level of smoothing improves the reliability of ToF predictions.

Deformation maps and the spatial distribution of selected MPs within each collapse source area are visible in Supplementary Materials.

4. Result

4.1. Mt-InSAR results

Satellite InSAR analysis of the five case studies reveals different deformation scenarios (Fig. 3). Cadia is the only case study to exhibit deformation a prolonged acceleration phase from January 2018, which culminated in the catastrophic failure of March 9, 2018.

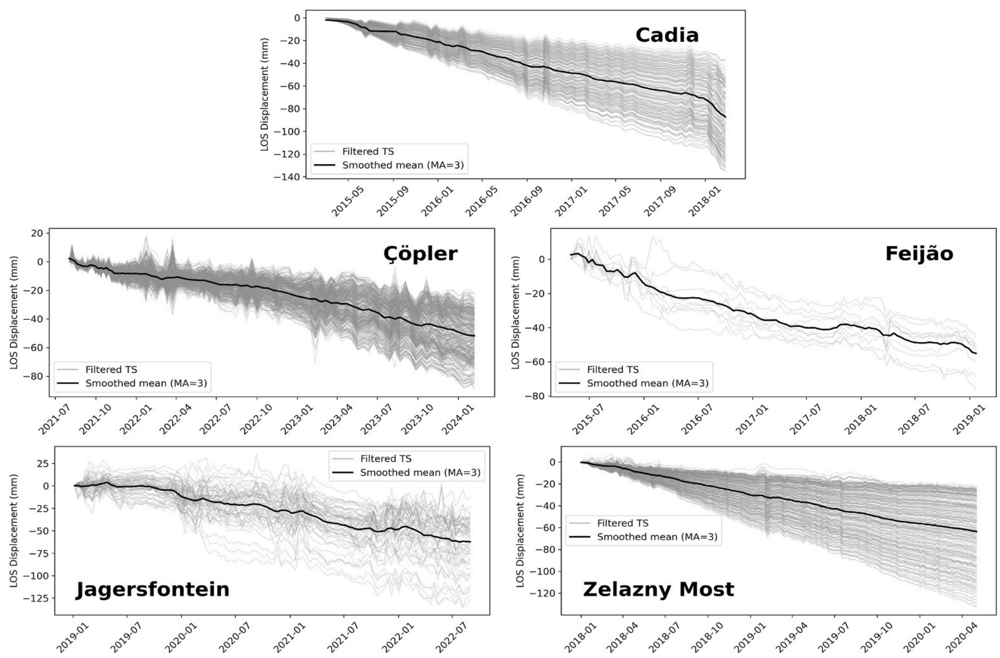

Fig. 3. InSAR LOS displacement time series of the five case studies In gray deformation trends of the MPs within the areas of collapse (in failure case studies) or of deformation (in the case of Zelazny Most). In black: mean time series of the area smoothed over a rolling window of 3 values.

Instead, Feijão and Jagersfontein show a more step-like time series, with stable phases alternating with unstable ones. In particular, Feijão seems to have experienced a subtle acceleration in the last period before failure. Çöpler shows a multi-stage acceleration time series with intense deformation and short windows of acceleration/deceleration. Lastly, Zelazny Most shows deformations that are more linear in time, aligning with a secondary creep behavior.

4.2. RA results

Table 4 summarizes the results of the RA analysis and the corresponding evaluation obtained using the Early Alert framework. Among the five case studies considered, only the Cadia case reaches the Failure Trend threshold before the actual failure. This trend is activated on February 25, 2018, providing a lead time of approximately 12 days prior to failure. In the remaining case studies, no consistent Failure Trend is ever reached prior to the collapse.

Furthermore, in the Zelazny case, the RAF algorithm never activates an alert, corresponding in fact to the only instance in which no failure actually occurred.

In this study, persistent alerts are defined as alerts sustained for more than three consecutive acquisition timestamps. Short-lived or intermittent alerts were more prone to false positives.

Table 4
Summary of RAS and RAF alert periods. Only long-lasting alerts (persisting for more than three consecutive acquisition intervals) are reported.

Name	# acq.	RAS - Yellow	RAS- Red	RAF - Yellow	RAF - Red	Failure Trend	Note from comparative investigations
Cadia	81	—	Feb 2018–failure	Aug –Oct 2017; Jan 2018–failure	Nov 2016 –Apr 2017; Jan –Feb 2018	Reached on Feb 25, 2018 until failure (TP)	Major construction activities at the dam site coincident with alert periods: (i) Feb–Jul 2017: construction of a 3-m embankment at the failure location; (ii) Dec 2017–Mar 2018: buttress construction; (iii) Jan 2018: toe excavation exposing weak foundation layers (remaining open until failure). [a] Persistent movements during 2017 also reported by independent studies. [b]
Çöpler	87	Mar – Dec 2023	Dec 2022 –Jan 2023; Mar - Jul 2023; Sep - Oct 2023	—	May –Sep 2023	Reached 30 May – 3 Sep (FP)	No precursor signal detected by InSAR prior to failure. The landslide is reported to have occurred very rapidly[c], likely exceeding the detecting capabilities of satellite InSAR monitoring.
Feijão	108	Jul –Aug 2018.	Oct 2017 –Feb 2018; Mar –Apr 2018 May –Jun 2018	Jan - Apr 2017; Jan –May 2018	Jan –Apr 2018; Dec 2018 – failure	Reached Jan 27 - Apr 21, 2018 (FP)	Construction and drilling activities at the dam from late 2017, including installation of Deep Horizontal Drains and boreholes. On June 11, 2018, a serious drilling-related incident produced visible mudflows. Seasonal rainfall coincided with some deformation accelerations.[d] The failure was rapid (flow liquefaction of contractive tailings), and no clear precursory acceleration was detected by monitoring systems prior to collapse.[e]
Jagersfontein	110	—	Jan- Feb 2020; Feb –Mar 2020; Jul –Sep 2021	Oct 2021 – Feb 2022	Dec 2020–Mar 2021	Reached on Feb 24–Mar 08, 2021 (FP)	High-resolution satellite imagery indicates progressive instability well before failure[f]: first signs in Feb 2019; significant movements during Jan–May 2020 (~17.5 m) associated with loading; migration of the southern wall toe from Aug 2020 to Feb 2021 (~14 m); crack-like features (~25 cm wide) observed in Sep 2020; continued southward movement through early 2022 (~10 m). Dam closure occurred between 2020 and June 2021.
Zelazny Most	139	Apr –Aug 2019; Feb – Mar 2020	Apr –May 2019 Jun - Aug 2019	—	—	No failure trend reached (TN)	A linear trend of steadily increasing deformation was observed[g]. No failure occurred.

[a] (Jefferies et al., 2019).
[b] (Carlà et al., 2019a; Thomas et al., 2019; Bayaraa et al., 2022).
[c] (Büyükakpınar et al., 2025).
[d] (Robertson et al., 2019).
[e] (Arroyo and Gens, 2021).
[f] (*Study into the Causes of the Jagersfontein Fine Tailings Storage Dam Failure on September 11, 2022*, 2024).
[g] (Sciortino et al., 2021).

4.2.1. Cadia NTSF

RA results from both forecasting algorithms applied to Cadia indicate that FS increases and SEM decreases from January 2018 up to the March 9, 2018 failure (Fig. 4b-d). In the RAF, such a risk increase is more persistent, thereby triggering a red alert on January 08, 2018, i.e., 61 days before failure (Fig. 4e).

With RAS, a short downgrade of the FS ('low risk') on February 01, 2018, doesn't let the alert be activated. Nevertheless, over the next two timestamps, the risk of failure increases from moderate to high, culminating in the failure trend on February 25, 2018, i.e., 12 days before the catastrophic collapse. Moreover, alerts would also have been triggered from the end of 2016 to mid-2017, and again from August 2017 to October 2017.

4.2.2. Çöpler HLF

For the Çöpler case study, two major periods of alert are identified (Fig. 5). The first, uniquely identified by RAS, from December 01, 2022 to January 6, 2023. The second, identified by both RAS, with a persistent (8-month-long) yellow/red alert period, from 19 March to November 26, 2022 and with RAF, from 30 May to September 3, 2023. Therefore, a three-month high-confidence alert would have been reached from 30 May to September 03, 2023.

4.2.3. Feijão

The results for the Feijão case study show distinct FS behaviors across the forecasting algorithms applied (Fig. 6).

The RAS algorithm identifies a high to very-high risk period extending from July 2017 to June 2018, characterized by a continuous increase in FS. During this interval, the SEM exhibits a sharp decrease between October 11, 2017 and February 08, 2018, indicating convergence of model predictions. This behavior triggered the longest red-alert period (approximately four months) detected in the analysis, occurring about one year prior to the failure (Fig. 6b-c).

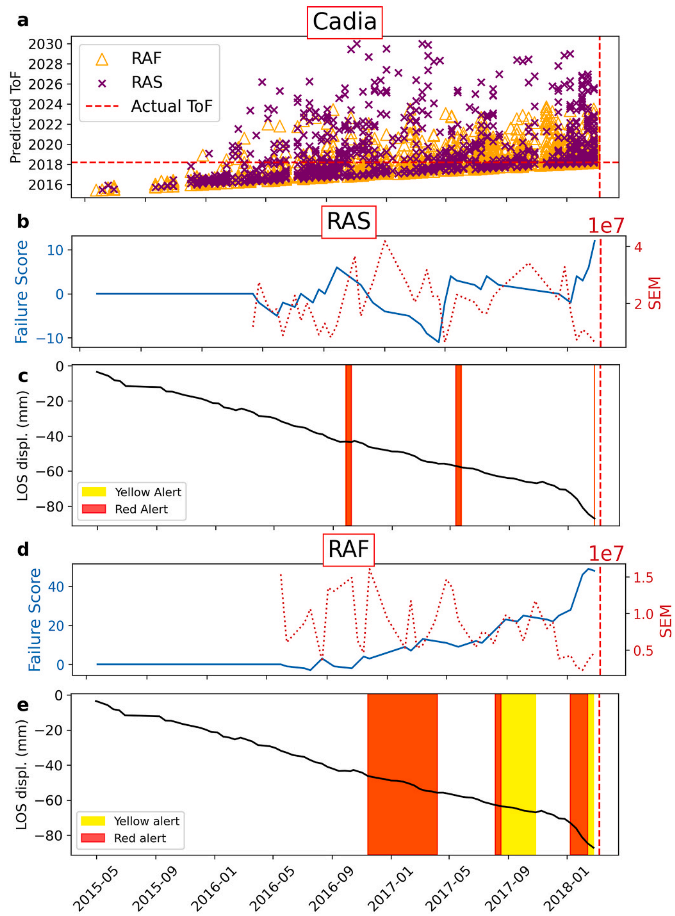

Fig. 4. Reiterative Algorithm results for the Cadia case study. (a) Prediction plot showing estimated failure times (y-axis) obtained using both algorithms (RAS and RAF) at each time of prediction (x-axis). (b–d) Temporal evolution of failure risk expressed through the Failure Score (FS) and the Standard Error of the Mean (SEM) for RAS (b) and RAF (d). (c–e) Early Alert algorithm results, where alerts are automatically derived from FS (yellow alert) and SEM (red alert). Alerts are superimposed on LOS displacement time series, which were used as input to the Reiterative Algorithm in a "simulated" prospective manner (see Section 2.8 'Simulated' prospective analysis for details).

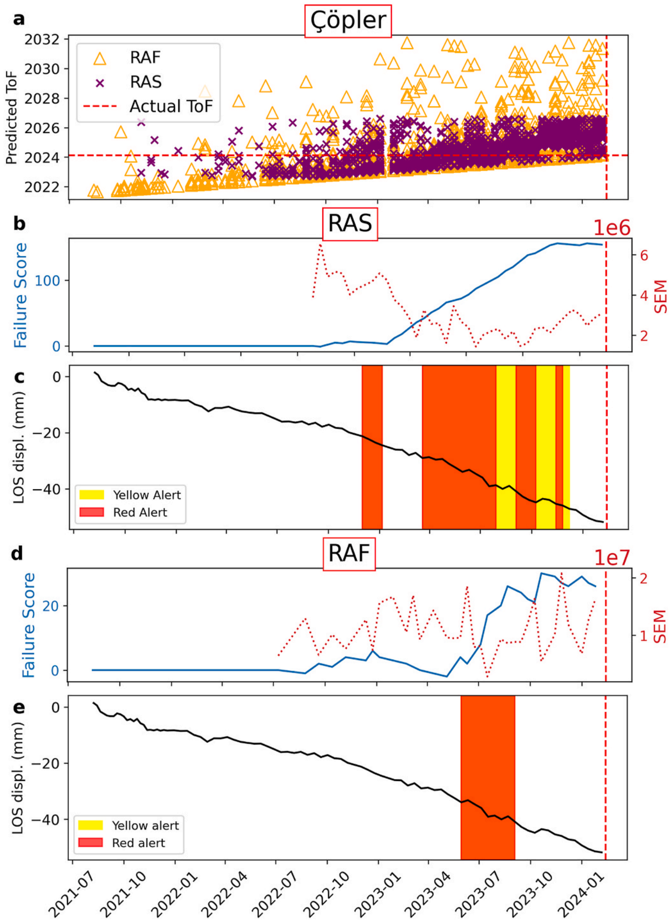

Fig. 5. Reiterative Algorithm results for the Çöpler case study. Panels and symbols are as in Fig. 4. Temporal evolution of Failure Score (FS), Standard Error of the Mean (SEM), and corresponding alert levels obtained using the RAS and RAF algorithms.

The RAF algorithm detects increased failure risk during three distinct time windows in the last three years preceding collapse: January 20–April 02, 2017, January 27 – April 21, 2018, and December 17, 2018 to failure. Although these alerts are not intermittent or short-lived, the SEM remains elevated and widely distributed across these periods, undermining forecast reliability. A persistent Failure Trend would have been reached from January 27 to April 21, 2018 (Fig. 6e).

4.2.4. Jagersfontein

RAS results for Jagersfontein show three persistent red alert periods: the first from January to February 2020, the second from February to March 2021, and the third from July to September 2021. The FS increases and decreases intermittently (Fig. 7b), with two pronounced peaks accompanied by a decrease in the SEM during the abovementioned first and third alert periods (Fig. 7c). In the period immediately preceding failure, the FS remains low and exhibits a linear decreasing trend, while the SEM remains high, indicating the absence of a clear pre-failure pattern.

Using the RAF algorithm, a persistent red alert period is detected from late December 2020 to early March 2022 (Fig. 7d-e) and is followed by a yellow alert from late October 2021 to early February 2022. Among these alerts, a concurrent FS increase and SEM decrease are observed only during the initial red alert period, suggesting greater confidence.

4.2.5. Zelazny Most

At Zelazny Most, RA predictions are highly scattered and associated with large SEM values, indicating substantial noise in the forecasting outputs (Fig. 8). Using the RAF algorithm, no alert level is reached during the monitored period (Fig. 8d-e).

In contrast, the RAS algorithm shows an increase in FS, accompanied by a decrease in SEM, between late April and early August 2019 (Fig. 8b-c). Outside such interval, FS values remain low with high SEM, suggesting limited forecasting confidence.

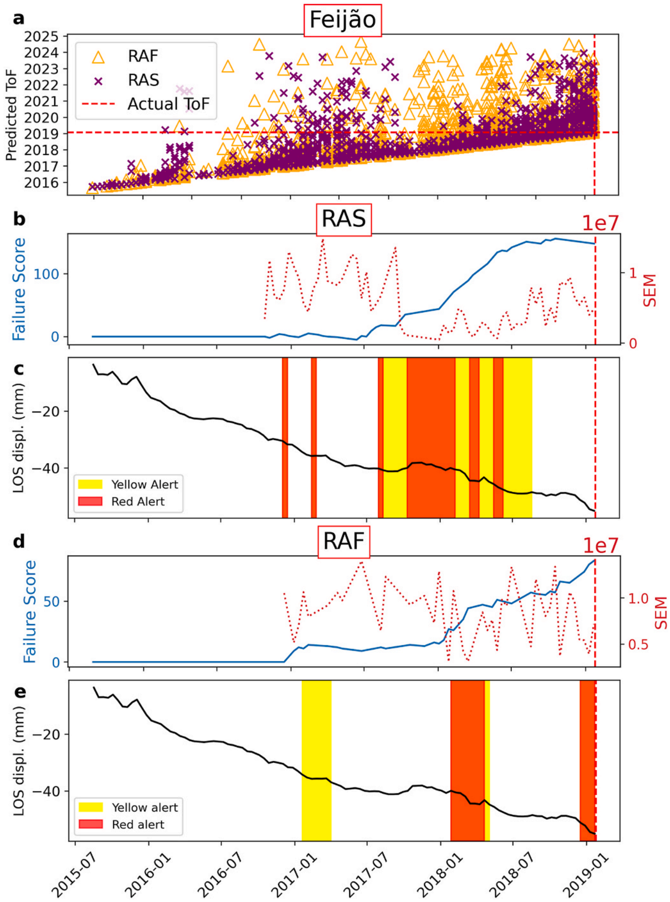

Fig. 6. Reiterative Algorithm results for the Feijão case study. Panels and symbols are as in Fig. 4. Temporal evolution of Failure Score (FS), Standard Error of the Mean (SEM), and corresponding alert levels obtained using the RAS and RAF algorithms.

5. Discussion

5.1. Limitations in data and methods

Before discussing the alerts detected with RA and the comparison with physical interpretations and published studies for the five case studies, the main limitations of the data and methodology are addressed.

5.1.1. Sensitivity of the RA early alert framework and false positives

The RA early alert framework is designed for early-warning applications in complex, highly heterogeneous systems, both natural and anthropogenic, such as landslides, TSFs, and HLFs. In such contexts, to detect early signs of impending failure, the algorithm must be calibrated to be sufficiently sensitive in order to avoid missing failures. As a consequence, the complete elimination of False Positives (FPs) is not possible (Chen and Jiang, 2020), whereas false negatives—cases in which a failure occurs without detection—must be strictly avoided.

As shown in Table 1, during the RA validation and FS threshold calibration phase, all failure cases were successfully identified, with no failures passing unnoticed. This corresponds to True Positive (TP) detections for all failure events, with lead times of weeks to months prior to collapse. Concerning the non-failure cases, in all instances, no failure trend was detected, thereby enhancing the robustness of RA.

However, in some instances, failures are anticipated by a single TP alert, whereas in others, additional FPs are also identified. Due to its iterative nature, the RA framework performs better (i.e., with a higher TPs/FPs) when fewer monitoring points are used as input. Instead, when a very large number of monitoring points is considered, the algorithm may be overwhelmed by the volume of predictions and struggle to distinguish convergence driven by real acceleration from signal artifacts, thereby activating many FPs alerts.

To limit alert fluctuations, as stated in the Methodology, an alert is issued only when activation conditions persist for at least two consecutive acquisition timestamps, and alert status changes are permitted only after two consecutive confirmations. While this strategy reduces oscillations, RA results indicate that many FPs persist also for more than only two consecutive timestamps. Increasing

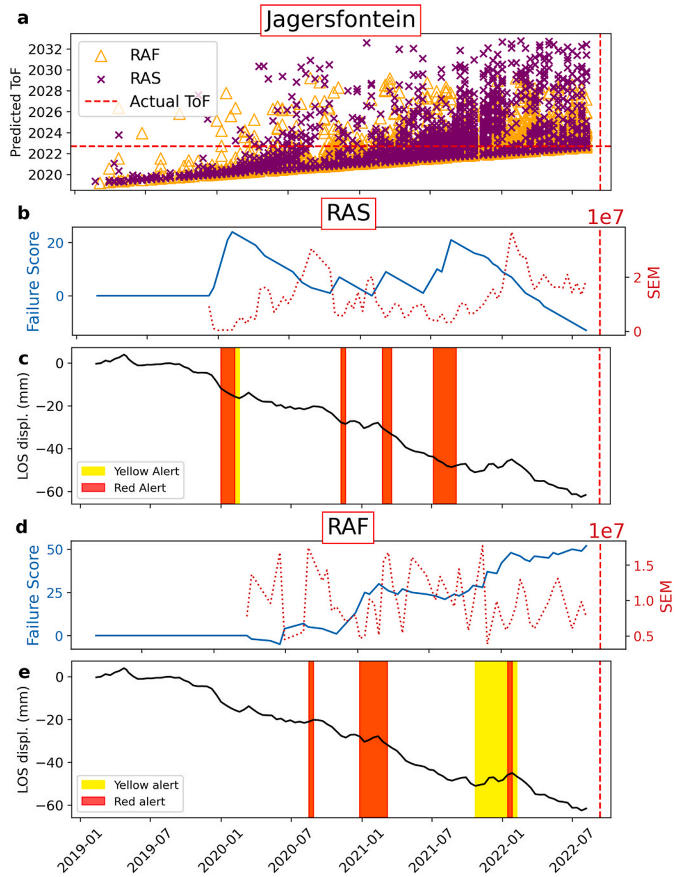

Fig. 7. Reiterative Algorithm results for the Jagersfontein case study. Panels and symbols are as in Fig. 4. Temporal evolution of Failure Score (FS), Standard Error of the Mean (SEM), and corresponding alert levels obtained using the RAS and RAF algorithms.

this persistence threshold could further reduce false positives; however, it would also increase the minimum time required to detect an accelerating trend (see Cadia with RAS, indeed increasing this threshold would not have detected any pre-failure alert). This fact underscores the need to reach a trade-off in calibrating thresholds. Furthermore, it highlights how increasing the temporal resolution of the monitoring sensor can greatly benefit the prompt detection of acceleration via RA, and consequently, the issuance of alerts. Furthermore, given the impossibility of completely eliminating FPs, we consider long alerts, those defined as persistent, to be more relevant than short ones.

5.1.2. Ambiguity between consolidation and instability-related deformation

Another limitation arises from the inability to unambiguously distinguish between consolidation-driven deformation and instability-related movement when only line-of-sight InSAR measurements are used. Indeed, without reconstructing the horizontal and vertical deformation components, it is not possible to separate vertical movement —often associated with long-term consolidation processes—from horizontal movement, which is generally more critical for structural instability.

Nevertheless, if the detected deformation were dominated by primary consolidation, a decelerating trend would be expected. In such a case, predictions obtained with RA—built to identify accelerating (hyperbolic-like) trends—would progressively lose convergence. This provides additional justification for assigning greater weight to persistent alerts, which are less likely to be associated with consolidation processes than short-lived or intermittent signals.

The objective of this study is to evaluate the potential of prediction methods based on tertiary creep for assessing instabilities in TSFs and HLFs, rather than providing a detailed physical interpretation of the radar signals associated with deformation processes. In this context, we refer to previous studies that, where possible, have reconstructed three-dimensional displacement components using remote sensing techniques and have provided detailed physical interpretations of the observed signals.

As the aim of this work is to test whether minor accelerations preceding collapse could have been detected, we developed a rapid hazard screening framework whose reliability is evaluated here. Through a comparative analysis with documented case studies and the relevant literature, we assess whether the detected alerts correspond to significant deformation processes. Conversely, in cases where alerts were not detected, we examine whether this is due to limitations of the methodology or to constraints related to data acquisition.

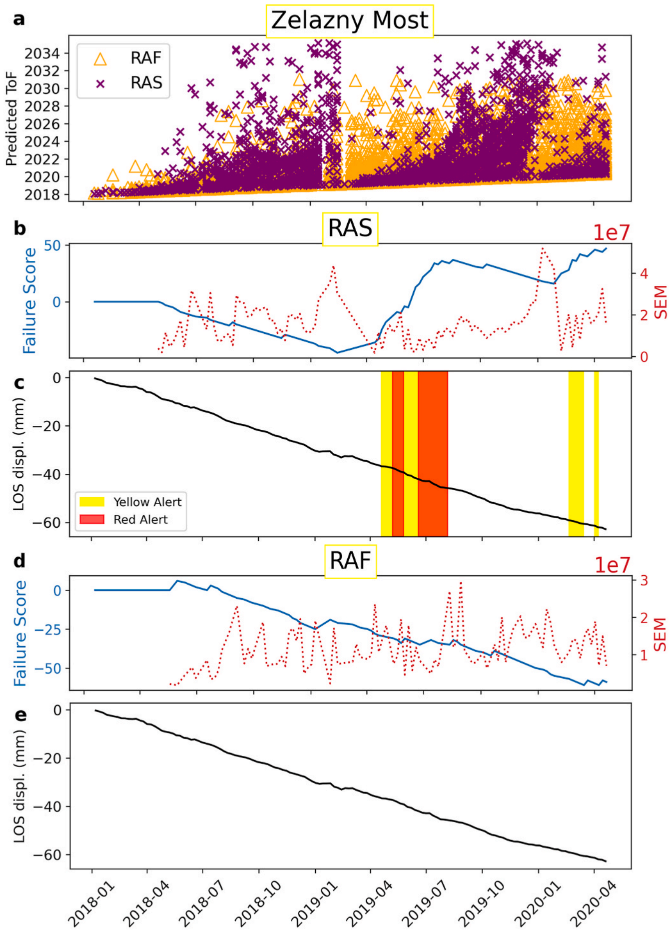

Fig. 8. Reiterative Algorithm results for the Zelazny Most case study. Panels and symbols are as in Fig. 4. Temporal evolution of Failure Score (FS), Standard Error of the Mean (SEM), and corresponding alert levels obtained using the RAS and RAF algorithms.

5.2. *Discussion of the results*

5.2.1. *Cadia NTSF*

Using the convergence of predictions as a proxy for future failure and its confidence, we demonstrate that it was possible to issue a moderate confidence alert for Cadia up to 2 months in advance, and a high confidence Failure Trend, 12 days before the collapse. Moreover, persistent alerts are identified by the RA from November 2016 to April 2017, Notably, both periods coincide with intense construction activities carried out at the dam collapse site. Specifically, on February 27, 2017, construction of a 3-m-high embankment began and continued until July 2017, while from December 15, 2017 to March 5, 2018, additional works involving buttress construction and excavation at the dam toe were undertaken (Jefferies et al., 2019). These activities exposed weak foundation layers and have likely increased stress and reduced the mechanical strength of the tailings, promoting unstable conditions within the dam structure.

Such instability is reflected in increased acceleration of the monitored materials, which was effectively captured by the forecasting algorithms. In fact, the RAF algorithm promptly identifies January 8, 2018 as the onset of prediction convergence, marked by a sharp increase in FS and a simultaneous decrease in SEM, indicating increasing failure risk. The RAS algorithm also exhibits a similar FS and SEM behavior during this period, despite minor short-term decreases.

The uniqueness of this alert sequence, compared with other false-positive detections, lies in the persistence of the signal: both the FS increase and the SEM decrease are sustained for more than four consecutive monitoring intervals. Given the 12-day satellite revisit time, this corresponds to a period exceeding one and a half months. This behavior ultimately led to the activation of the Failure Trend on February 25, 2018, providing a lead time of approximately 12 days that could have facilitated hazard identification and risk mitigation.

Importantly, a direct observation of the NTSF on the morning of 9 March revealed extensive cracking within the dam body, a symptom of an emerging failure mechanism. As a result, the affected area was promptly evacuated, and no injuries nor losses were reported. Overall, this outcome highlights the potential operational value of the proposed forecasting framework in supporting timely decision-making and risk management, as well as the essential role of in-situ monitoring. Moreover, the RAF red alert detected on 8 January is consistent with previous work which identifies the onset of final deformation in late January 2018 (Thomas et al., 2019).

5.2.2. Cöpler

The deformation that led to the Çöpler landslide was localized using seismic inversion analysis and was assessed as very rapid, making it very challenging to detect by satellite InSAR analyses (Büyükakpınar et al., 2025). Consequently, the failure was not captured by the RA. Concerning alerts generations, the algorithms identified several different periods, including a Failure Trend that terminated approximately five months before the failure. Although wide cracks were reported some hours before failure (Petley, 2024), no warning was issued, to the authors' knowledge. Furthermore, detailed public reports on the failure and on the monitoring of the HLF are not available. As a result, a comprehensive comparative assessment of observed failure precursors and RA outputs was not conducted in this study.

5.2.3. Feijão

The Feijão case study is particularly relevant, as numerous investigations have examined the failure and its causes remain debated (Robertson et al., 2019; Arroyo and Gens, 2021; Zhu et al., 2024; Reid et al., 2025). The peculiar deformation signal observed prior to the collapse led some scholars to conclude that the failure was foreseeable using inverse-velocity method (Grebby et al., 2021). However, other studies have confined such signal to InSAR noise (Holden et al., 2020). Within the interpretative framework proposed by Robertson et al. (2019), which attributes failure to rainfall-related suction loss and creep, the timing of RAF alerts would appear consistent with seasonal precipitation patterns. However, the SEM during these periods remains high and noisy, indicating low forecast reliability.

The only period during which the SEM exhibits a clear linear decrease—indicating convergence of predictions and increased confidence—is observed for the RAS algorithm between October 11, 2017 to February 08, 2018. Notably, this interval is slightly offset from the emergent risk period identified by Das et al. (2024) as being within an emergent risk of failure (February 27, 2018 - August 28, 2018). However, our model does not determine the 'imminent risk of failure' highlighted by the cited authors, which is reported to be up to December 2018. Conversely, the RAS algorithm detects a red alert on December 17, 2018, approximately 39 days prior to failure. Such a period is consistent with the ~40-day pre-failure warning period reported by (Grebby et al., 2021). However, also in this case, the associated SEM values remain high and scattered, suggesting that the confidence in the failure prediction was low.

5.2.4. Jagersfontein

The alerts detected by the RA for Jagersfontein case, appear to coincide with periods of intense activity at the dam. Notably, the first red alert detected by the RAS algorithm from January to March 2020 coincides with significant weight placement on the dam, as observed from high-resolution satellite imagery during the period January to May 2020 (Study into the Causes of the Jagersfontein Fine Tailings Storage Dam Failure on September 11, 2022, 2024).

Furthermore, red alerts detected by RAF (August 2020) and RAS (November 2020), although short-lived, were issued during a period when ~25 cm-wide cracks developed in the area that later collapsed, as documented by satellite imagery dated September 24, 2020. During this period, from August 2020 to the end of February 2021, intense southward migration of the toe of the southern wall was observed, quantified from pre- and post-event imagery to be ~14 m.

Notably, the RAF algorithm also detects a persistent red alert during this period, from December 2020 to March 2021, characterized by concurrent increases in the FS and decreases in the SEM. Within this interval, between 24 February and March 8, 2021, the Failure Trend threshold was also reached, corresponding to the highest level of confidence in the alerts.

Additional satellite imagery from February 2021 and January 2022 indicates further large southward displacement of the dam toe, estimated at approximately 10 m. This phase is highlighted by the RA through a red alert detected by RAS between July and September 2021, and by RAF slightly later, from October 2021 to February 2022.

Following these alert periods, the RA does not detect further acceleration, and the final failure passes unnoticed by the forecasting framework, resulting in a hazardous false negative. However, very large displacements of the dam toe on the order of tens of meters in the months and years preceding failure (Perdikou and Lees, 2023), may have limited the detectability of deformation from SAR signals.

Rapid loading of coarse tailings under undrained conditions likely limited pore water dissipation and reduced the shear strength of the underlying fine tailings. This can promote the sliding along the interface between coarse and fine tailings (*Study into the Causes of the Jagersfontein Fine Tailings Storage Dam Failure on September 11, 2022*, 2024). Furthermore, the presence of a large supernatant pond in close proximity to the embankment detected was detected from satellite imagery (Cacciuttolo and Cano, 2023; Torres-Cruz and O'Donovan, 2023). These processing wastewaters could have exacerbated tailings mobility. These factors collectively contribute to rapid instability mechanisms which are inherently challenging to detect with satellite InSAR techniques.

5.2.5. Zelazny Most

The linear constant deformation observed at Zelazny Most may reflect normal settlement of fine tailings (Mazzanti et al., 2021; Sciortino et al., 2021). RAS detect alerts from April and August 2019. As the mine was operational and possible stabilization measures could have been taken a systematic evaluation of the alarm's validity is not possible. Moreover, the absence of alerts from the RAF algorithm and its highly scattered forecasts, suggests that the detected alerts should be interpreted with caution and are likely attributable to FPs.

5.3. Implications for monitoring

In unconsolidated, loose and contractive materials such as tailings, failure can be so sudden that it cannot be grasped by satellite InSAR revisit time of 6-12 days. Indeed, the final acceleration phase may be measured in minutes/second rather than hours/days, thus it may be very challenging to detect. ToF forecasting remains complex because the characteristic time scale of deformation may be shorter than the monitoring sensor revisit time.

In this context, monitoring TSFs and HLFs from satellite platforms could greatly benefit from the combined use of complementary techniques. An example is pixel tracking of optical imagery, which can detect faster movements that may not be measurable using satellite InSAR alone, as demonstrated by recent studies (Handwerger et al., 2025).

Despite this limitation, accelerating deformation trends may still develop over longer periods prior to failure. The Cadia case supports the potentiality of using classical forecasting methods, such as RA, using satellite SAR images. Nevertheless, Cadia appears to represent a favorable case, and for more effective hazard assessment in general, increased temporal data acquisition is needed. This could be achieved, for example, by using near real-time instruments like Ground-Based InSAR (GB-InSAR), which would increase the likelihood of detecting pre-failure deformations, thus providing valuable insights into the predictability of a failure.

6. Conclusions

In summary, this work (a) demonstrates the potential of satellite monitoring for an initial, cost-effective large-scale screening of TSFs and HLFs; (b) introduces a modified RA methodology that advances previous implementations by issuing prospective warnings and quantifying the predictions confidence; (c) highlights the importance of different monitoring systems that could deliver precious informations for rapidly evolving failures; (d) demonstrates that different forecasting method yield different yet meaningful information that can increase forecasting confidence.

Continued advances in satellite acquisition frequency and in forecasting approaches together with the development of methods that explicitly account for the physical dynamics of failure, are expected to improve failure forecasting capabilities. In addition the integration of complementary sensors—such as pixel offset tracking from optical satellite imagery and satellite InSAR—together with near real-time monitoring techniques, as GB-InSAR, could significantly enhance the monitoring of large structures such as TSFs and HLFs. The combination of complementary techniques with automated forecasting frameworks, such as RA, represents a promising direction for future research in collapse detection, as it may improve both detection capability and the reliability of early warning confidence.

CRediT authorship contribution statement

Stefano Szakolczai: Writing – original draft, Visualization, Software, Methodology, Investigation, Formal analysis, Conceptualization. **Luca Piciullo:** Writing – review & editing, Validation, Investigation. **Regula Frauenfelder:** Writing – review & editing, Data curation. **Malte Vöge:** Writing – review & editing, Data curation. **Tommaso Carlà:** Writing – review & editing, Supervision. **Emanuele Intrieri:** Writing – review & editing, Supervision, Conceptualization, Methodology.

Ethics in publishing statement

This research presents an accurate account of the work performed, all data presented are accurate and methodologies detailed enough to permit others to replicate the work.

This manuscript represents entirely original works and or if work and/or words of others have been used, that this has been appropriately cited or quoted and permission has been obtained where necessary.

This material has not been published in whole or in part elsewhere.

The manuscript is not currently being considered for publication in another journal.

That generative AI and AI-assisted technologies have not been utilized in the writing process or if used, disclosed in the manuscript the use of AI and AI-assisted technologies and a statement will appear in the published work.

That generative AI and AI-assisted technologies have not been used to create or alter images unless specifically used as part of the research design where such use must be described in a reproducible manner in the methods section.

All authors have been personally and actively involved in substantive work leading to the manuscript and will hold themselves jointly and individually responsible for its content.

Declaration of competing interest

The authors declare that they have no known competing financial interests or personal relationships that could have appeared to influence the work reported in this paper.

Acknowledgments

This article was partly produced with the support of a scholarship financed by the Piano Nazionale di Ripresa e Resilienza—PNRR "Geosciences IR" Project—IR0000037 (Mission 4 "Education and Research"—Component 2 "From Research to Business"- Investment 3.1, "Fund for the realisation of an integrated system of research and innovation infrastructures") financed by European Union

NextGenerationEU. The study was also supported by the project "SP12 - Towards sustainable mine tailings", internally financed by the Norwegian Geotechnical Institute (NGI) and through NGI's base funding from The Research Council of Norway. The authors would like to thank the numerous anonymous reviewers, whose insightful comments and suggestions helped improve and clarify the manuscript. We extend our sincere thanks to Leinauer et al., (2023) , for making their collection of slope deformation data up to failure openly accessible.

Appendix A. Supplementary data

Supplementary data to this article can be found online at https://doi.org/10.1016/j.rsase.2026.101963.

Data availability

Data will be made available on request.

References

Arroyo, M., Gens, A., 2021. Computational analyses of Dam I failure at the Corrego de Feijao mine in Brumadinho. Final Rep. VALE SA.
Barde, M.P., Barde, P.J., 2012. What to use to express the variability of data: standard deviation or standard error of mean? Perspect. Clin. Res. 3.
Bayaraa, M., Sheil, B., Rossi, C., 2022. InSAR and numerical modelling for tailings dam monitoring – the Cadia failure case study. Geotechnique 1–19. https://doi.org/10.1680/jgeot.21.00399, 0.
BBC, 2024. Turkey mine: "race against time" to free workers after landslide. BBC News. URL. https://www.bbc.com/news/world-europe-68292469 (accessed 6.12.24).
Berardino, P., Fornaro, G., Lanari, R., Sansosti, E., 2002. A new algorithm for surface deformation monitoring based on small baseline differential SAR interferograms. IEEE Trans. Geosci. Rem. Sens. 40, 2375–2383. https://doi.org/10.1109/TGRS.2002.803792.
Bowker, L.N., Chambers, D.M., 2015. The risk, public liability, & economics of tailings storage facility failures. Earthwork Act 24, 1–56.
Brawner, C.O., Stacey, P.F., 1979. Hogarth pit slope failure, Ontario, Canada. In: Voight, Barry (Ed.), Rockslides and Avalanches. Elsevier, pp. 691–707.
Brown, I., Hittinger, M., Goodman, R., 1980. Finite element study of the Nevis Bluff (New Zealand) rock slope failure. Rock Mech. Felsmech. Mec. Roches 12, 231–245. https://doi.org/10.1007/BF01251027.
Büyükakpınar, P., Carrillo-Ponce, A.C., Munir, M.B., Karasözen, E., Tanyas, H., Ertuncay, D., Palliath, A., Gorum, T., 2025. Seismic, field, and remote sensing analysis of the 13 February 2024 çöpler gold mine landslide, Erzincan, Türkiye. Seism. Rec. 5, 165–174.
Cacciuttolo, C., Cano, D., 2023. Spatial and temporal study of supernatant process water pond in tailings storage facilities: use of remote sensing techniques for preventing mine tailings dam failures. Sustainability 15, 4984. https://doi.org/10.3390/su15064984.
Calò, M., Ruggieri, S., Nettis, A., Uva, G., 2024. A MTInSAR-Based early warning system to appraise deformations in simply supported concrete girder bridges. Struct. Control Health Monit. 2024, 8978782. https://doi.org/10.1155/2024/8978782.
Cambridge, M., Shaw, D., 2019. Preliminary reflections on the failure of the Brumadinho tailings dam in January 2019. Dams Reservoirs 29, 113–123. https://doi.org/10.1680/jdare.19.00004.
Carlà, T., Intrieri, E., Di Traglia, F., Nolesini, T., Gigli, G., Casagli, N., 2017. Guidelines on the use of inverse velocity method as a tool for setting alarm thresholds and forecasting landslides and structure collapses. Landslides 14, 517–534. https://doi.org/10.1007/s10346-016-0731-5.
Carlà, T., Intrieri, E., Raspini, F., Bardi, F., Farina, P., Ferretti, A., Colombo, D., Novali, F., Casagli, N., 2019a. Perspectives on the prediction of catastrophic slope failures from satellite InSAR. Sci. Rep. 9, 14137. https://doi.org/10.1038/s41598-019-50792-y.
Carlà, T., Nolesini, T., Solari, L., Rivolta, C., Dei Cas, L., Casagli, N., 2019b. Rockfall forecasting and risk management along a major transportation corridor in the Alps through ground-based radar interferometry. Landslides 16, 1425–1435. https://doi.org/10.1007/s10346-019-01190-y.
Carmo, Flávio Fonseca do, Kamino, L.H.Y., Junior, R.T., Campos, I.C. de, Carmo, Felipe, Fonseca do, Silvino, G., Castro, K.J., da, S.X. de, Mauro, M.L., Rodrigues, N.U.A., Miranda, M.P. de S., Pinto, C.E.F., 2017. Fundão tailings dam failures: the environment tragedy of the largest technological disaster of Brazilian mining in global context. Perspect. Ecol. Conserv. 15, 145–151. https://doi.org/10.1016/j.pecon.2017.06.002.
Casagli, N., Intrieri, E., Tofani, V., Gigli, G., Raspini, F., 2023. Landslide detection, monitoring and prediction with remote-sensing techniques. Nat. Rev. Earth Environ. 4, 51–64. https://doi.org/10.1038/s43017-022-00373-x.
Chen, M., Jiang, Q., 2020. An early warning system integrating time-of-failure analysis and alert procedure for slope failures. Eng. Geol. 272, 105629. https://doi.org/10.1016/j.enggeo.2020.105629.
Clarkson, L., Williams, D., Seppälä, J., 2021. Real-time monitoring of tailings dams. Georisk Assess. Manag. Risk Eng. Syst. Geohazards 15, 113–127.
Dai, C., Li, W., Wang, D., Lu, H., Xu, Q., Jian, J., 2021. Active landslide detection based on Sentinel-1 data and InSAR technology in Zhouqu County, Gansu Province, Northwest China. J. Earth Sci. 32, 1092–1103. https://doi.org/10.1007/s12583-020-1380-0.
Dai, K., Li, Z., Xu, Q., Bürgmann, R., Milledge, D.G., Tomas, R., Fan, X., Zhao, C., Liu, X., Peng, J., 2020. Entering the era of earth observation-based landslide warning systems: a novel and exciting framework. IEEE Geosci. Remote Sens. Mag. 8, 136–153.
Das, S., Priyadarshana, A., Grebby, S., 2024. Monitoring the risk of a tailings dam collapse through spectral analysis of satellite InSAR time-series data. Stoch. Environ. Res. Risk Assess. https://doi.org/10.1007/s00477-024-02713-3.
Davies, M., 2002. Tailings impoundment failures: are geotechnical engineers listening? Waste Geotech 20, 1–36.
Duan, H., Li, Y., Jiang, H., Li, Q., Jiang, W., Tian, Y., Zhang, J., 2023. Retrospective monitoring of slope failure event of tailings dam using InSAR time-series observations. Nat. Hazards 117, 2375–2391.
Famiglietti, N.A., Miele, P., Defilippi, M., Cantone, A., Riccardi, P., Tessari, G., Vicari, A., 2024. Landslide mapping in calitri (Southern Italy) using new multi-temporal InSAR algorithms based on permanent and distributed scatterers. Remote Sens. 16, 1610. https://doi.org/10.3390/rs16091610.
Ferretti, A., Fumagalli, A., Novali, F., Prati, C., Rocca, F., Rucci, A., 2011. A new Algorithm for processing interferometric Data-stacks: SqueeSAR. IEEE Trans. Geosci. Rem. Sens. 49, 3460–3470. https://doi.org/10.1109/TGRS.2011.2124465.
Festa, D., Bonano, M., Casagli, N., Confuorto, P., De Luca, C., Del Soldato, M., Lanari, R., Lu, P., Manunta, M., Manzo, M., Onorato, G., Raspini, F., Zinno, I., Casu, F., 2022. Nation-wide mapping and classification of ground deformation phenomena through the spatial clustering of P-SBAS InSAR measurements: italy case study. ISPRS J. Photogrammetry Remote Sens. 189, 1–22. https://doi.org/10.1016/j.isprsjprs.2022.04.022.
Franks, D.M., Stringer, M., Torres-Cruz, L.A., Baker, E., Valenta, R., Thygesen, K., Matthews, A., Howchin, J., Barrie, S., 2021. Tailings facility disclosures reveal stability risks. Sci. Rep. 11, 5353. https://doi.org/10.1038/s41598-021-84897-0.
Fukuzono, T., 1985. A new method for predicting the failure time of slope. Presented at the Proceedings, 4th Int'L. Conference and Field Workshop on Landslides, pp. 145–150.
Gama, F., Mura, J.C., Paradella, W.R., de Oliveira, C.G., 2020. Deformations prior to the brumadinho dam collapse revealed by Sentinel-1 InSAR data using SBAS and PSI techniques. Remote Sens. 12. https://doi.org/10.3390/rs12213664.

Gigli, G., Fanti, R., Canuti, P., Casagli, N., 2011. Integration of advanced monitoring and numerical modeling techniques for the complete risk scenario analysis of rockslides: the case of mt. Beni (Florence, Italy). Eng. Geol. 120, 48–59. https://doi.org/10.1016/j.enggeo.2011.03.017.

Grebby, S., Sowter, A., Gluyas, J., Toll, D., Gee, D., Athab, A., Girindran, R., 2021. Advanced analysis of satellite data reveals ground deformation precursors to the Brumadinho Tailings Dam collapse. Commun. Earth Environ. 2, 2. https://doi.org/10.1038/s43247-020-00079-2.

Handwerger, A.L., Lacroix, P., Bell, A.F., Booth, A.M., Huang, M.-H., Mudd, S.M., Bürgmann, R., Fielding, E.J., 2025. Multi-sensor remote sensing captures geometry and slow-to-fast sliding transition of the 2017 Mud Creek landslide. Sci. Rep. 15, 29831. https://doi.org/10.1038/s41598-025-11399-8.

Hayashi, S., Yamamori, T., 1991. Forecast of time-to-slope failure by the a-tr method. Landslides 28, 1–8. https://doi.org/10.3313/jls1964.28.2_1.

Holden, D., Donegan, S., Pon, A., 2020. Brumadinho Dam InSAR study: analysis of TerraSAR-X, COSMO-SkyMed and Sentinel-1 images preceding the collapse. In: Dight, P., Dight, P. (Eds.), Presented at the Slope Stability 2020: 2020 International Symposium on Slope Stability in Open Pit Mining and Civil Engineering, Australian Centre for Geomechanics, pp. 293–306. Perth.

Hooper, A., 2008. A multi-temporal InSAR method incorporating both persistent scatterer and small baseline approaches. Geophys. Res. Lett. 35. https://doi.org/10.1029/2008GL034654.

Hudson-Edwards, K.A., Kemp, D., Torres-Cruz, L.A., Macklin, M.G., Brewer, P.A., Owen, J.R., Franks, D.M., Marquis, E., Thomas, C.J., 2024. Tailings storage facilities, failures and disaster risk. Nat. Rev. Earth Environ. 5, 612–630. https://doi.org/10.1038/s43017-024-00576-4.

Intrieri, E., Carlà, T., Gigli, G., 2019. Forecasting the time of failure of landslides at slope-scale: a literature review. Earth Sci. Rev. 193, 333–349. https://doi.org/10.1016/j.earscirev.2019.03.019.

Intrieri, E., Gigli, G., 2016. Landslide forecasting and factors influencing predictability. Nat. Hazards Earth Syst. Sci. Discuss 16, 1–10. https://doi.org/10.5194/nhess-16-2501-2016.

Intrieri, E., Gigli, G., Mugnai, F., Fanti, R., Casagli, N., 2012. Design and implementation of a landslide early warning system. Eng. Geol. 147–148, 124–136. https://doi.org/10.1016/j.enggeo.2012.07.017.

Intrieri, E., Meng, Q., Tofani, V., 2021. KLC2020 implementation: challenges for the development of satellite landslide early warning systems. Landslides 18, 3499–3502. https://doi.org/10.1007/s10346-021-01721-6.

Intrieri, E., Raspini, F., Fumagalli, A., Lu, P., Del Conte, S., Farina, P., Allievi, J., Ferretti, A., Casagli, N., 2018. The Maoxian landslide as seen from space: detecting precursors of failure with Sentinel-1 data. Landslides 15, 123–133. https://doi.org/10.1007/s10346-017-0915-7.

Ishwar, S.G., Kumar, D., 2017. Application of DInSAR in mine surface subsidence monitoring and prediction. Curr. Sci. 112, 46. https://doi.org/10.18520/cs/v112/i01/46-51.

Jefferies, M., Morgenstern, N.R., Van Zyl, D., John Wates, 2019. Report on NTSF Embankment Failure Cadia Valley Operations for Ashurst Australia. Independent Technical Review Board.

Kossoff, D., Dubbin, W.E., Alfredsson, M., Edwards, S.J., Macklin, M.G., Hudson-Edwards, K.A., 2014. Mine tailings dams: characteristics, failure, environmental impacts, and remediation. Appl. Geochem. 51, 229–245. https://doi.org/10.1016/j.apgeochem.2014.09.010.

Lacroix, P., Dini, B., Cheaib, A., 2022. Measuring kinematics of slow-moving landslides from satellite images. Surf. Displac. Meas. Remote Sens. Images 315–338.

Lanari, R., Reale, D., Bonano, M., Verde, S., Muhammad, Y., Fornaro, G., Casu, F., Manunta, M., 2020. Comment on "Pre-Collapse Space Geodetic Observations of Critical Infrastructure: The Morandi Bridge, Genoa, Italy" by Milillo et al. (2019). Remote Sens. 12 (24), 4011. https://doi.org/10.3390/rs12244011.

Leinauer, J., Weber, S., Cicoira, A., Beutel, J., Krautblatter, M., 2023. An approach for prospective forecasting of rock slope failure time. Commun. Earth Environ. 4, 253. https://doi.org/10.1038/s43247-023-00909-z.

Manconi, A., 2021. How phase aliasing limits systematic space-borne DInSAR monitoring and failure forecast of alpine landslides. Eng. Geol. 287, 106094.

Marais, L., Kemp, D., Watt, P. van der, Matebesi, S., Cloete, J., Harris, J., Ern, M.A.L., Owen, J.R., 2024. The catastrophic failure of the Jagersfontein tailings dam: an industrial disaster 150 years in the making. Int. J. Disaster Risk Reduct., 104585 https://doi.org/10.1016/j.ijdrr.2024.104585.

Massonnet, D., Rabaute, T., 1993. Radar interferometry: limits and potential. IEEE Trans. Geosci. Rem. Sens. 31, 455–464. https://doi.org/10.1109/36.214922.

Mazzanti, P., Antonielli, B., Sciortino, A., Scancella, S., Bozzano, F., 2021. Tracking deformation processes at the legnica glogow copper district (Poland) by satellite insar—Ii: żelazny most tailings dam. Land 10, 654.

Milillo, P., Giardina, G., Perissin, D., Milillo, G., Coletta, A., Terranova, C., 2019. Pre-Collapse Space Geodetic Observations of Critical Infrastructure: The Morandi Bridge, Genoa, Italy. Remote Sens. 11 (12), 1403. https://doi.org/10.3390/rs11121403.

Mirmazloumi, S.M., Wassie, Y., Nava, L., Cuevas-González, M., Crosetto, M., Monserrat, O., 2023. InSAR time series and LSTM model to support early warning detection tools of ground instabilities: mining site case studies. Bull. Eng. Geol. Environ. 82, 374. https://doi.org/10.1007/s10064-023-03388-w.

Motsau, B., van Wyk, D., 2022. Report on the Jagersfontein Tailings Disaster.

Mufundirwa, A., Fujii, Y., Kodama, J., 2010. A new practical method for prediction of geomechanical failure-time. Int. J. Rock Mech. Min. Sci. 47, 1079–1090. https://doi.org/10.1016/j.ijrmms.2010.07.001.

Navarro, J.A., Tomás, R., Barra, A., Pagán, J.I., Reyes-Carmona, C., Solari, L., Vinielles, J.L., Falco, S., Crosetto, M., 2020. ADAtools: automatic detection and classification of active deformation areas from PSI displacement maps. ISPRS Int. J. GeoInf. 9, 584. https://doi.org/10.3390/ijgi9100584.

Perdikou, S., Lees, A., 2023. Could regular satellite InSAR monitoring have helped prevent the Jagersfontein Tailings Dam failure?. In: Proceedings of 76th Canadian Geotechnical Society Annual Conference. Presented at the GeoSaskatoon (2023), Canadian Geotechnical Society.

Petley, D., 2024. Precursory deformation for the landslide at Çöpler Mine in Turkey [WWW Document]. Eos. URL. http://eos.org/thelandslideblog/copler-mine-4 (accessed 2.3.25).

Piciullo, Luca, Storrøsten, Erlend Briseid, Liu, Zhongqiang, Nadim, Farrokh, Lacasse, Suzanne, 2022. A new look at the statistics of tailings dam failures. Eng. Geol. 303, 106657. ISSN 0013-7952. https://doi.org/10.1016/j.enggeo.2022.106657.

Rana, N.M., Delaney, K.B., Evans, S.G., Deane, E., Small, A., Adria, D.A.M., McDougall, S., Ghahramani, N., Take, W.A., 2024. Application of Sentinel-1 InSAR to monitor tailings dams and predict geotechnical instability: practical considerations based on case study insights. Bull. Eng. Geol. Environ. 83, 204. https://doi.org/10.1007/s10064-024-03680-3.

Raspini, F., Bianchini, S., Ciampalini, A., Del Soldato, M., Solari, L., Novali, F., Del Conte, S., Rucci, A., Ferretti, A., Casagli, N., 2018. Continuous, semi-automatic monitoring of ground deformation using Sentinel-1 satellites. Sci. Rep. 8, 7253. https://doi.org/10.1038/s41598-018-25369-w.

Raspini, F., Caleca, F., Del Soldato, M., Festa, D., Confuorto, P., Bianchini, S., 2022. Review of satellite radar interferometry for subsidence analysis. Earth Sci. Rev. 235, 104239.

Reid, D., Arroyo, M., Jefferies, M., Gens, A., Fourie, A., Mánica, M., 2025. Alternative views on the soil mechanics relevant for the Feijao failure. In: Proceedings of Tailings and Mine Waste 2025.

Robertson, P.K., de Melo, L., Williams, D.J., Wilson, G.W., 2019. Report of the Expert Panel on the Technical Causes of the Failure of Feijão Dam I.

Rose, N.D., Hungr, O., 2007. Forecasting potential rock slope failure in open pit mines using the inverse-velocity method. Int. J. Rock Mech. Min. Sci. 44, 308–320. https://doi.org/10.1016/j.ijrmms.2006.07.014.

Rotta, L.H.S., Alcântara, E., Park, E., Negri, R.G., Lin, Y.N., Bernardo, N., Mendes, T.S.G., Filho, C.R.S., 2020. The 2019 Brumadinho tailings dam collapse: possible cause and impacts of the worst human and environmental disaster in Brazil. Int. J. Appl. Earth Obs. Geoinformation 90, 102119. https://doi.org/10.1016/j.jag.2020.102119.

Ryan, T.M., Call, RichardD., 1992. Applications of rock mass monitoring for stability assessment of pit slope failure. In: Rock Mechanics. Balkema, Rotterdam, pp. 221–229.

Saito, M., 1969. Forecasting time of slope failure by tertiary creep. Presented at the Proceedings of the 7th International Conference on Soil Mechanics and Foundation Engineering, pp. 677–683. Mexico City, Mexico.

Saito, M., Uezawa, H., 1961. Failure of soil due to creep. Proc. 5th Int. Conf. Soil Mech. Found. Eng.

Sciortino, A., Antonielli, B., Scancella, S., Bozzano, F., Mazzanti, P., Moretto, S., 2021. Satellite InSAR for assessing deformation processes at the Zelazny Most Tailings Dam (Poland). Presented at the 7th International Conference on Tailings Management.

Sharifi, S., Macciotta, R., Hendry, M.T., 2024. Critical assessment of landslide failure forecasting methods with case histories: a comparative study of INV, MINV, SLO, and VOA. Landslides. https://doi.org/10.1007/s10346-024-02237-5.
Solari, L., Del Soldato, M., Raspini, F., Barra, A., Bianchini, S., Confuorto, P., Casagli, N., Crosetto, M., 2020. Review of satellite interferometry for landslide detection in Italy. Remote Sens. 12, 1351.
Sousa, J.J., Bastos, L., 2013. Multi-temporal SAR interferometry reveals acceleration of bridge sinking before collapse. Nat. Hazards Earth Syst. Sci. 13, 659–667. https://doi.org/10.5194/nhess-13-659-2013.
Study into the Causes of the Jagersfontein, 2024. Study into the Causes of the Jagersfontein Fine Tailings Storage Dam Failure on 11 September 2022 (No. Revision 1), . . University of Pretoria and University of the Witwatersrand, Departments of Civil Engineering.
Su, C., Mergili, M., Rana, N.M., Zhang, S., Dai, C., Wang, B., Han, Y., 2024. Failure analysis and flow dynamic modeling using a new slow-flow functionality: the 2022 Jiaokou (China) tailings dam breach. Landslides 21, 379–391. https://doi.org/10.1007/s10346-023-02146-z.
Suwa, H., Mizuno, T., Ishii, T., 2010. Prediction of a landslide and analysis of slide motion with reference to the 2004 Ohto slide in Nara, Japan. Geomorphology 124, 157–163. https://doi.org/10.1016/j.geomorph.2010.05.003.
Tavenas, F., Leroueil, S., 1981. Creep and failure of slopes in clays. Can. Geotech. J. 18, 106–120.
Thomas, A., Edwards, S., Engels, J., McCormack, H., Hopkins, V., Holley, R., 2019. Earth observation data and satellite InSAR for the remote monitoring of tailings storage facilities: a case study of Cadia Mine, Australia. In: Paterson, A.J.C., Fourie, A., Reid, D., Paterson, A.J.C., Fourie, A., Reid, D. (Eds.), Presented at the Paste 2019: 22Nd International Conference on Paste, Thickened and Filtered Tailings. Australian Centre for Geomechanics, Perth, pp. 183–195.
Tordesillas, A., Zheng, H., Qian, G., Bellett, P., Saunders, P., 2024. Augmented intelligence forecasting and what-if-scenario analytics with quantified uncertainty for big real-time slope monitoring data. IEEE Trans. Geosci. Rem. Sens. 62, 1–29. https://doi.org/10.1109/TGRS.2024.3382302.
Torres-Cruz, L.A., O'Donovan, C., 2023. Public remotely sensed data raise concerns about history of failed Jagersfontein dam. Sci. Rep. 13, 4953. https://doi.org/10.1038/s41598-023-31633-5.
Voight, B., 1988. A method for prediction of volcanic eruptions. Nature 332, 125–130. https://doi.org/10.1038/332125a0.
Yamaguchi, U., Shimotani, T., 1986. A case study of slope failure in a limestone quarry. Int. J. Rock Mech. Min. Sci. Geomech. Abstr. 23, 95–104. https://doi.org/10.1016/0148-9062(86)91670-0.
Yukon, 2024. Victoria Gold Corporation's eagle mine heap leach failure [WWW Document]. URL. https://yukon.ca/en/victoria-gold-corporations-eagle-mine-heap-leach-failure (accessed 2.4.25).
Zebker, H.A., Villasenor, J., 1992. Decorrelation in interferometric radar echoes. IEEE Trans. Geosci. Rem. Sens. 30, 950–959. https://doi.org/10.1109/36.175330.
Zhang, J., Tang, H., Zhang, X., Wu, Q., Zhang, W., Su, X., Fang, K., 2025. A generalized phenomenological approach for real-time automatic time of failure forecasting of landslides. Eng. Geol. 356, 108303. https://doi.org/10.1016/j.enggeo.2025.108303.
Zhu, F., Zhang, W., Puzrin, A.M., 2024. The slip surface mechanism of delayed failure of the Brumadinho tailings dam in 2019. Commun. Earth Environ. 5, 33. https://doi.org/10.1038/s43247-023-01086-9.

Further reading

Zhou, X.-P., Liu, L.-J., Xu, C., 2020. A modified inverse-velocity method for predicting the failure time of landslides. Eng. Geol. 268, 105521. https://doi.org/10.1016/j.enggeo.2020.105521.
Zhou, S., Tordesillas, A., Intrieri, E., Di Traglia, F., Qian, G., Catani, F., 2022. Pinpointing early signs of impending slope failures from space. J. Geophys. Res. Solid Earth 127. https://doi.org/10.1029/2021JB022957.